


U-Net-based hybrid framework for accelerating deterministic rough-surface mixed lubrication simulations

Filimonas Kaliafets¹, Suhaib Ardah¹, James P. Ewen^{1,2}, Daniele Dini¹

¹Department of Mechanical Engineering, Imperial College London, Exhibition Road, South Kensington, London, SW7 2AZ, United Kingdom

²Department of Mechanical Engineering, University of Bath, Claverton Down, Bath BA2 7AY, United Kingdom

 Corresponding author. E-mail: f.kaliafets23@imperial.ac.uk

Abstract:

Despite significant advances in deterministic mixed lubrication modelling, the computational complexity of these simulations remains prohibitive, limiting their practical use in rapid analysis and design optimisation. This study addresses this bottleneck by developing a hybrid machine learning framework that integrates artificial neural networks (ANNs) and convolutional neural networks (CNNs), specifically U-Nets, into a classical finite volume mixed lubrication solver to accelerate rough surface simulations without sacrificing fidelity. The approach uses ANNs to predict smooth pressure, film thickness, and temperature fields from operating conditions, while U-Nets reconstruct rough fields from smooth solutions and rough surface topographies. The ANNs achieve high accuracy for smooth fields, with mean R_{rs}^2 values of 0.998 for pressure, 0.999 for film thickness, and 0.925 for temperature. The U-Nets generalise well to rough surfaces, achieving R_{rs}^2 values of 0.990, 0.996, and 0.938 for pressure, film thickness, and temperature respectively. Six hybrid configurations are assessed, all of which reduce computational cost relative to the classical solver (average simulation time: 10.36 minutes). The most efficient framework delivers a 72.85% reduction in computation time across all testing samples. Overall, the results demonstrate that hybrid

27 machine learning-physics frameworks can substantially accelerate deterministic mixed lubrication
28 simulations while preserving high predictive accuracy.

29

30 **Keywords: Thermo-elastohydrodynamic lubrication, Mixed lubrication, Surface roughness,**
31 **Convolutional neural networks, U-Nets**

32 **1. Introduction**

33 Thermo-elastohydrodynamic lubrication (TEHL) simulations have long been used to accurately model
34 tribological contacts in bearings, gears and other components and mechanisms. TEHL theory extends
35 classical lubricated contact modelling by coupling hydrodynamic fluid film behaviour and elastic
36 deformation of solid bodies with thermal effects arising from viscous dissipation and material conductivity.
37 Traditional TEHL simulations solve a set of nonlinear partial differential equations, including the Reynolds
38 equation, elasticity equations and energy equations, to predict pressure, film thickness and temperature
39 profiles, among others, with high fidelity [1].

40

41 A central challenge in TEHL modelling is the accurate representation of real surface topography. For
42 idealised smooth surfaces, the Reynolds equation predicts a continuous pressurised fluid film that entirely
43 separates the contacting solids. However, in practice, surface roughness often has characteristic scales that
44 are comparable, or even exceed, the film thickness predicted for smooth surfaces, particularly under severe
45 operating conditions. Moreover, in recent years there has been a significant push towards lower viscosity
46 lubricants, particularly in the automotive sector, to minimise power losses and improve energy efficiency
47 [2]. Although lower viscosity lubricants reduce viscous friction losses, they also tend to produce thinner
48 lubricant films, increasing the likelihood of mixed lubrication conditions in which asperity interactions
49 occur. Under these conditions, the accurate modelling of roughness effects in tribological contacts becomes
50 more important than ever.

51

52 Substantial research effort has been devoted to the development of deterministic mixed lubrication models
53 capable of explicitly resolving surface roughness effects representative of real engineering surfaces. Unlike
54 stochastic roughness approaches, deterministic models directly incorporate measured or generated surface
55 topography into the numerical solution of the lubrication problem [3]. Ai and Cheng [4] used a deterministic
56 approach to model moving surface defects in heavily loaded point contacts with good agreement against
57 experimental results. Chang [5] used a deterministic model to simulate the contact of two colliding

58 asperities as well as the contact between two rough surfaces with sinusoidal roughness profiles in the mixed
59 lubrication regime. Hu and Zhu [6] employed a unified deterministic model to simulate various lubrication
60 conditions, from full-film elastohydrodynamic lubrication down to boundary lubrication in point contacts.
61 Their approach was based on the idea that the same Reynolds equation may be used for both the
62 hydrodynamic and contact regions. Their model proved to be able to provide solutions even at very low
63 film thickness ratios (λ). Subsequent studies further extended deterministic approaches to include thermal
64 effects, transient operating conditions and more complex surface geometries [3], [7].

65

66 Substantial advances have also been made in the numerical methods used in lubrication models. Efficient
67 discretisation strategies, multigrid methods, fast Fourier transform techniques and advanced iterative
68 solvers have significantly improved solution robustness and convergence behaviour [8], [9], [10], [11].
69 Nevertheless, the complexity of such simulations means that the computational burden remains significant
70 [12]. The multiscale nature of rough surface lubrication problems requires fine spatial discretisation in order
71 to accurately resolve asperity-scale interactions while simultaneously capturing the overall contact
72 behaviour. In addition, the inclusion of thermal effects introduces further nonlinear coupling between
73 temperature-dependent lubricant properties, heat generation and hydrodynamic effects. Furthermore, the
74 inclusion of transient effects compounds these challenges, as the above calculations have to be repeated for
75 individual time iterations. As a result, high-fidelity deterministic lubrication simulations usually require
76 substantial computational resources and long execution times, limiting their applicability real-time
77 engineering applications such as digital twins and online condition monitoring systems.

78 Machine learning models have been rapidly emerging as a way to accelerate such simulations, due to their
79 near-instantaneous prediction capability once trained. More specifically, machine learning has been used to
80 predict friction coefficients, wear rates, film thickness and pressure distributions, as well as to develop
81 surrogate models for elastohydrodynamic and thermo-elastohydrodynamic lubrication problems [13], [14],
82 [15], [16], [17]. Physics-informed neural networks (PINNs) have also been explored in this context. These
83 embed governing physical equations directly into the learning process, enabling the solution of lubrication-
84 related partial differential equations without fully explicit numerical discretisation [18], [19], [20].

85

86 However, the majority of existing machine learning approaches in lubrication modelling have focused on
87 idealised or nominally smooth contact conditions, where surface topography is either neglected or
88 represented in a simplified manner. Comparatively limited attention has been given to the application of
89 machine learning techniques to rough surface simulations, particularly in the context of deterministic TEHL
90 modelling where multiscale surface features significantly influence the tribological response of the system.
91 In addition, while PINNs offer a physics-driven alternative to purely data-driven models, their application
92 to elastohydrodynamic lubrication remains challenging due to the strong coupling between pressure and
93 elastic deformation, as well as difficulties in resolving steep gradients, enforcing boundary conditions, and
94 capturing complex multiscale behaviours [21]. Capturing rough surface interactions in general remains
95 particularly challenging due to the highly nonlinear coupling between roughness-induced pressure
96 perturbations, local film thickness variations and thermal effects. Nevertheless, recent developments
97 indicate that there is rapid progress in this area. In a recent study by Zhao et al. [22], the authors developed
98 an Adaptively Weighted Multi-Scale PINN framework that was able to accurately solve EHL problems for
99 smooth, periodically rough as well as fractal rough surfaces. However, the model was trained and evaluated
100 for specific operating conditions, limiting its general applicability across varying loads and speeds.

101

102 Another type of neural networks, convolutional neural networks (CNNs), have also been used in
103 applications where spatially varying fields have to be resolved and interpreted. CNNs contain convolution

104 kernels that are used to extract spatial features and detect patterns in the inputs [23]. The pooling layers
105 reduce the resolution of the feature maps (outputs of the convolutional layers) to achieve shift-invariance,
106 which allows the network to recognise features regardless of their actual location in the spatial domain.
107 However, a disadvantage of classic CNNs is that the downsampling process in the pooling layers can lead
108 to significant detail loss in the output [24]. To solve this problem U-Nets can be used.

109
110 U-Nets are a type of CNN typically extensively used in medical applications, primarily for image
111 segmentation [25], [26], [27]. These have an encoder-decoder type architecture. The encoder block is
112 similar to a classic CNN with convolution and pooling layers that downsample the feature maps to extract
113 high-level features. The decoder block is used to increase the resolution of the feature maps, restoring any
114 detail lost. Skip connections link corresponding encoder and decoder layers, allowing fine-grained details
115 lost during downsampling to be reintroduced into the decoder, improving the reconstruction of high-
116 resolution outputs [28]. This architecture enables U-Nets to capture both global and local features, which
117 is particularly important in applications such as tribology, where microscopic surface roughness interacts
118 with macroscopic pressure, film thickness and temperature fields.

119
120 The aim of this work is, therefore, to develop and evaluate a deep learning framework capable of predicting
121 rough-surface mixed lubrication field distributions from corresponding smooth-field solutions and surface
122 topography data. Specifically, a U-Net architecture is employed to learn the nonlinear spatial mapping
123 between smooth pressure, film thickness, and temperature profiles, combined with surface roughness
124 information, and the resulting rough-field responses. By doing so, this study seeks to provide a
125 computationally efficient surrogate model that retains spatial resolution while significantly reducing the
126 cost associated with deterministic rough surface mixed lubrication simulations.

2. Methodology

2.1. Unified lubrication framework

The details of the classical mixed lubrication framework used in this study are presented in [12] and [29]. In summary, the model is based on a unified finite volume formulation capable of resolving TEHL and mixed lubrication behaviour in both smooth and deterministic rough surface contacts. The framework solves the coupled generalised Reynolds and energy equations, while also accounting for mass-conserving cavitation, elastic deformation of the contacting bodies, and transient thermal effects in the lubricant and solids. A deterministic surface roughness description is incorporated directly into the film thickness, allowing asperity-level interactions and transition between full-film and asperity contact regimes to be captured within the same numerical formulation. The lubricant rheology is described using a pressure- and temperature-dependent viscosity model based on the Roelands equation, while density variations are captured using the Dowson–Higginson relationship. In addition, shear-thinning behaviour is accounted for using an Eyring-type non-Newtonian model. These constitutive relations enable accurate representation of lubricant behaviour under the high-pressure, high-shear, and thermally coupled conditions characteristic of mixed lubrication. The solution is obtained using a fully coupled iterative scheme with appropriate convergence criteria for pressure, temperature, and load balance, as described in detail in the above references.

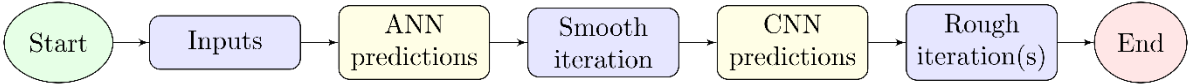
2.2. Acceleration of mixed lubrication model

In rough surface mixed lubrication simulations, the smooth solution is normally computed first, with the roughness profiles gradually introduced into the domain over a few time steps (for example 30 or 50 time steps according to Wang and Zhu [1]) to ensure stability. The fact that the solutions for many time steps have to be computed sequentially makes rough surface simulations time consuming. In this study, it is investigated whether the subsequent time steps can be skipped altogether, with a final solution obtained using a combination of the smooth profiles only and machine learning models.

153 In a previous study [12], artificial neural networks (ANNs) were used to predict key parameters in
154 tribological systems that were in turn used as initial predictions for the mixed lubrication models. In that
155 study only smooth surfaces were considered and the inputs to the ANNs were purely scalar values, like load
156 or entrainment speed. In this paper, that approach is extended to rough surfaces.

157
158 Predicting the results of rough surface mixed lubrication simulations with ANNs that can only accept scalar
159 values is impossible, since two rough surfaces can be very different even if they have the same root mean
160 square (RMS) roughness, skewness and kurtosis, all of which are parameters used to characterise such
161 rough surfaces. Therefore, conventional fully connected ANNs are unsuitable in this scenario.
162 Convolutional neural networks (CNNs), on the other hand, are more suitable since they are able to accept
163 images, or matrices, as inputs and are particularly useful for recognising spatial patterns [23].

164
165 In the proposed framework, the CNNs accept the pressure, film thickness, velocity and temperature profiles
166 from the smooth solution, as well as the final rough surface profiles, as inputs, and in turn output the rough
167 profiles of pressure, film thickness and temperature, either skipping the rough iterations altogether or using
168 such predictions to accelerate the rough iterations. ANNs are also used to accelerate the smooth iteration of
169 the solver in the manner described in [12]. A flowchart of the proposed hybrid framework is presented in
170 Figure 1.



171
172 *Figure 1 – Hybrid framework flowchart.*
173

174 More specifically, six different hybrid frameworks are compared. In all of them, as well as the classical
175 finite volume framework (Classical FW), only two time iterations are simulated. In the first time iteration
176 the surfaces are smooth and in the second time iteration the fully developed roughness profiles are
177 introduced into the simulation.

178 In Hybrid FW 1, 2 and 3 the first time iteration is run in the same way as the Classical FW, at the end of
179 which the CNN predictions take place. The differences between the frameworks are evident in the second
180 time iteration. In Hybrid FW 1, after the CNN predictions take place, the second time iteration is allowed
181 to run to completion. In Hybrid FW 2, the second time iteration is limited to just one global iteration. In
182 Hybrid FW 3, the second time iteration is skipped altogether and the CNN predictions make up the final
183 solution. In this way, varying amounts of acceleration and solution accuracy can be achieved. The final
184 three hybrid frameworks, Hybrid FW 1 (+ANN), Hybrid FW 2 (+ANN), Hybrid FW 3 (+ANN), are
185 identical to Hybrid FW 1, 2 and 3, respectively, but also include ANN predictions for smooth pressure, film
186 thickness and temperature profiles at the beginning of the first iteration, with the first iteration being allowed
187 to run to completion in the same manner as [12]. Table 1 shows a summary of the six different hybrid
188 frameworks.

189

190 Table 1: Hybrid simulation frameworks.

Framework	ANN prediction	Smooth iteration	CNN prediction	Rough iteration
Hybrid FW 1	No	Same as Classical FW	Yes	Same as Classical FW
Hybrid FW 2	No	Same as Classical FW	Yes	Limited to one global iteration
Hybrid FW 3	No	Same as Classical FW	Yes	Skipped
Hybrid FW 1 (+ANN)	Yes	Same as Classical FW	Yes	Same as Classical FW
Hybrid FW 2 (+ANN)	Yes	Same as Classical FW	Yes	Limited to one global iteration
Hybrid FW 3 (+ANN)	Yes	Same as Classical FW	Yes	Skipped

191

192 To quantify the amount of acceleration of each Hybrid FW simulation, the percentage difference is
193 calculated between the Hybrid FW simulation time and the Classical FW simulation time. The simulation
194 time is defined as the wall-clock time elapsed between the inputs being defined and global convergence

195 being reached and does not include any post-processing like file-saving. All simulations were performed
 196 using MathWorks MATLAB R2024a on a computer equipped with a 13th Gen Intel® Core™ i7-13850HX
 197 (base speed 2.10 GHz), 64 GB of RAM and running the Windows 11 Enterprise operating system.

198
 199 2.3. Training and testing data generation

200 In this study, both the operating conditions and individual roughness profiles are varied across the training
 201 and testing samples. These operating conditions varied include the applied load, entrainment speed and
 202 slide-to-roll ratio. The range of those values are chosen to reflect the range of operating conditions of a mini
 203 traction machine (MTM) [30]. The solid body and lubricant properties remain constant across all samples.
 204 Similarly to [12], the Latin Hypercube Sampling (LHS) method was used to sample data points with the
 205 desired range of values using the MATLAB function *lhsdesign*. The generated samples were categorised
 206 using the dimensionless load (M) and material (L) Moes parameters. The expressions for M and L for point
 207 contacts are given below [1]:

$$M = W^*(2U^*)^{-3/4} \tag{1}$$

$$L = G^*(2U^*)^{1/4} \tag{2}$$

208
 209 where $W^* = \frac{W}{E'R^2}$, $U^* = \frac{\eta_0 u_{ent}}{E'R}$ and $G^* = \alpha_p E'$.

210
 211 Table 2 shows the operating conditions varied across the samples and Table 3 shows the parameters
 212 remaining constant across all simulations.

213
 214 Table 2: Training and testing sample parameters.

Parameter	Min.	Max.
Applied load, W [N]	10	100
Entrainment speed, u_{ent} [m/s]	0.01	3
Slide-to-roll ratio, SRR [-]	0.1	2

215 This study is divided into three phases. In Phase 1, Gaussian isotropic rough surfaces with identical
216 statistical roughness parameters were used for training and testing. Although the statistical properties were
217 fixed, the specific roughness profiles differed between samples due to their random generation. In Phase 2,
218 the networks trained in Phase 1 were evaluated on Gaussian rough surfaces with varying Peklenik number
219 (γ) values in order to assess their ability to generalise across different surface anisotropies. Finally, in Phase
220 3, the trained networks were tested on Gaussian rough surfaces with varying root mean square (RMS)
221 roughness (R_q) values to evaluate their sensitivity to changes in roughness amplitude. In this way, the
222 predictive capability of the neural networks can be assessed both for interpolation within the trained
223 roughness distribution and for extrapolation to surfaces with modified statistical characteristics.

224 Table 3: Constant parameters.

Parameter type	Parameter	Value
Operating conditions	Ambient temperature, T_{amb} [°C]	30
Lubricant properties	Lubricant reference viscosity, η_0 [Pa·s]	0.05
	Lubricant pressure-viscosity coefficient, α_p [1/Pa]	2×10^{-8}
	Fluid specific heat capacity, c_p [J/(kg·K)]	2000
	Fluid thermal conductivity, k [W/(m·K)]	0.14
	Fluid coefficient of thermal expansion, β [1/K]	6.5×10^{-4}
	Eyring shear stress, τ_E [Pa]	1×10^{-7}
	Reference density, ρ_0 [kg/m ³]	875
Solid properties	Effective radius of curvature, R [m]	0.01
	Young's modulus of solid bodies, $E_{1,2}$ [Pa]	2×10^{11}
	Poisson's ratio of solid bodies, $\nu_{1,2}$ [-]	0.3
	Thermal conductivity of solid bodies, $k_{1,2}$ [W/(m·K)]	21
	Specific heat capacity of solid bodies, $c_{p1,2}$ [J/(kg·K)]	470
	Density of solid bodies, $\rho_{1,2}$ [kg/m ³]	7850
	Boundary friction coefficient, f_b [-]	0.1
Simulation parameters	Mesh size of fluid and solid domains, $N_x \times N_y \times N_z$	$64 \times 64 \times 11$
	Computational domain	$-1.9 \leq x/a \leq 1.1,$ $-1.5 \leq y/a \leq 1.5$
	Pressure, liquid film fraction convergence criterion, $e^{p,\theta}$	1×10^{-5}
	Load convergence criterion, e^W	1×10^{-4}
	Temperature convergence criterion, e^T	1×10^{-4}
	Global pressure convergence criterion, e_{global}^p	1×10^{-3}
	Global temperature convergence criterion, e_{global}^T	1×10^{-3}
	Number of time iterations, N_t	2
Time step magnitude, Δt [s]	$\Delta t = \Delta x / u_{ent}$	

225

226 In Phase 1, 2000 samples were generated, with 85% of them (1700 samples) used for training and 15%
 227 (300 samples) used for testing the accuracy of the predictions. Phases 2 and 3 consisted of 75 testing
 228 samples each. A summary of the roughness parameters of the surfaces used in the three phases is presented
 229 in Table 4.

230 Table 4: Roughness parameters.

Parameter	Phase 1	Phase 2	Phase 3
Root mean square roughness, $R_{q,1,2}$ [m]	1×10^{-7}	1×10^{-7}	$1 \times 10^{-8} - 1 \times 10^{-7}$
Skewness, $R_{sk,1,2}$ [-]	0	0	0
Kurtosis, $R_{ku,1,2}$ [-]	3	3	3
Correlation length in x-direction, $l_{x,1,2}^*$ [m]	5×10^{-5}	5×10^{-5}	5×10^{-5}
Peklenik number, $\gamma_{1,2} = l_{x,1,2}^*/l_{y,1,2}^*$ [-]	1	0.1 – 10	1

231
 232 While parameters such as RMS roughness and the Peklenik number provide convenient scalar descriptors
 233 of surface amplitude and anisotropy, they do not fully characterise the spatial frequency content of the
 234 surface. For this reason, the surface topographies are further described in terms of their power spectral
 235 density (PSD), which provides a frequency-domain representation of roughness and distinguishes
 236 contributions from different lengths scales.

237
 238 The importance of PSD-based characterisation has been highlighted in recent surface metrology studies,
 239 which emphasise that conventional roughness parameters alone are insufficient to uniquely define surface
 240 topography. In particular, the Surface-Topography Challenge study [31] demonstrated the necessity of
 241 spectral analysis for meaningful comparison and reproducibility of rough surfaces. Accordingly, PSD
 242 spectra of the generated surfaces in the training and testing samples are presented in Section 3.1 to provide
 243 a more complete description of their multiscale characteristics. These were calculated using the method
 244 described in [31].

245 2.4. Machine learning models

246 2.4.1 Artificial neural networks

247 In this study, ANNs were used for the prediction of the smooth profiles of pressure, film thickness and
248 temperature. Their use is motivated by previous work by the authors [12], in which they demonstrated
249 strong predictive capability for smooth TEHL problems using scalar operating parameters as inputs.

250
251 Three separate ANNs were constructed in MATLAB for smooth pressure, film thickness and temperature
252 field predictions. The ANNs consisted of multiple hidden layers, each made up of a
253 *fullyConnectedLayer*, a *swishLayer* and a *dropoutLayer* to avoid overfitting. The scalar inputs were
254 passed to the ANNs using a *featureInputLayer* with a feature size equal to the number of input
255 parameters (three). A final *fullyConnectedLayer* with size equal to the number of output values of each
256 ANN is used in addition to a *regressionLayer* to handle the outputs. The adaptive moment estimation
257 (ADAM) algorithm is used for training the ANNs as was done in [12].

258
259 Due to the small number of scalar inputs and their comparable magnitudes across the sampled operating
260 range, additional input normalisation was not required in the present study. This differs from the approach
261 adopted in [12], where normalisation was necessary due to the inclusion of additional parameters spanning
262 several orders of magnitude. For example, Young's modulus varied between 70×10^9 and 400×10^9 Pa while
263 the lubricant pressure–viscosity coefficient ranged between 1×10^{-8} and 2.5×10^{-8} Pa⁻¹.

265 2.4.2 Convolutional neural networks

266 In this study, the U-Nets were constructed in MATLAB using the built-in *unet* function. Three separate U-
267 Nets were constructed for rough pressure, film thickness and temperature field predictions. The inputs were
268 passed to the U-Nets using an *imageInputLayer* allowing the spatial fields to be treated as two-
269 dimensional images. The profiles from the smooth solution used as inputs to the U-Nets implicitly capture

270 the variations within the training and testing space, as changes in operating conditions are directly reflected
 271 in their spatial distributions. These inputs are summarised in Table 5.

272

273 Table 5: U-Net inputs.

U-Net	Input	Normalisation	Type
	Target roughness profile	$(s_1 + s_2)R/a^2$	One 2D matrix ($N_x \times N_y$)
	Smooth pressure profile	p/p_{Hertz}	One 2D matrix ($N_x \times N_y$)
All	Smooth temperature profile	$\ln(T/T_{amb})$	Multiple 2D matrices $N_z \times (N_x \times N_y)$
	Smooth fluid velocity profile in x-direction	u_f/u_{ent}	Multiple 2D matrices $N_z \times (N_x \times N_y)$
Pressure / temperature	Smooth film thickness profile	hR/a^2	One 2D matrix ($N_x \times N_y$)
Film thickness	Smooth film thickness profile	$(h - h_{macro})R/a^2,$ where $h_{macro} = \frac{x^2}{2R} + \frac{y^2}{2R}$	One 2D matrix ($N_x \times N_y$)

274

275 The inputs to the pressure and temperature U-Nets were identical. However, the smooth film thickness
 276 profile input to the film thickness U-Net was modified slightly by removing its macroscale geometry
 277 component. This was done because the macroscopic film thickness variation has a significantly larger
 278 magnitude than the roughness-induced perturbations within the Hertzian contact region. As a result, that
 279 macroscale component can dominate the loss function during training and reduce the network's sensitivity
 280 to the smaller-scale variations that are of primary interest. By subtracting the macroscale geometry, the
 281 network was encouraged to focus on learning the roughness-induced deviations in film thickness within the
 282 contact region, improving predictive accuracy where it is most critical.

283 This modification was not applied to the pressure and temperature networks, as the rough pressure and
 284 temperature fields are predominantly governed by their corresponding smooth distributions combined with
 285 the surface roughness effects. In those cases, the smooth field provides the appropriate large-scale structure
 286 for the prediction, and its magnitude does not mask the local roughness-induced variations in the same
 287 manner observed for film thickness.

288

289 2.4.3 Hyperparameter optimisation

290 To ensure optimal network performance, the hyperparameters of the ANNs were systematically tuned using
 291 Bayesian optimisation. Bayesian optimisation iteratively evaluates different hyperparameter combinations
 292 and uses the results of previous iterations to guide the selection of new candidates, focusing the search on
 293 regions of the hyperparameter space that are likely to improve performance [32]. This approach is more
 294 efficient than random or grid search methods and is particularly useful when training neural networks is
 295 computationally expensive.

296

297 The objective of the optimisation was to maximise the predictive accuracy of each network, represented by
 298 the mean rescaled coefficient of determination (R_{rs}^2) of the testing dataset across all samples. The parameter
 299 R_{rs}^2 is defined as

$$R_{rs}^2 = \frac{1}{2-R^2}, \quad (3)$$

300

301 where R^2 is the conventional coefficient of determination

$$R^2 = 1 - \frac{\sum_i (y_i - \hat{y}_i)^2}{\sum_i (y_i - \bar{y})^2}, \bar{y} = \frac{1}{N} \sum_{i=1}^N y_i. \quad (4)$$

302

303 Here, y_i is the actual value of a variable, \hat{y}_i is the predicted NN value and N is the number of output values
 304 of each NN for each sample. For example, for 2D profiles (pressure and film thickness) $N = N_x \times N_y =$
 305 $64 \times 64 = 4,096$ and for 3D profiles $N = N_x \times N_y \times N_z = 64 \times 64 \times 11 = 45,056$. The use of a rescaled

coefficient of determination ensures that the performance metric remains bounded between 0 and 1, avoiding the misleading interpretation of negative R^2 values.

For the ANNs, the optimisation explored the number of hidden layers, the number of neurons per hidden layer, and the dropout rate. For the U-Nets, the encoder depth, which determines the number of times the input image is downsampled and upsampled, was varied from 3 to 5, while the number of filters in the first encoder layer were varied from 16 to 64. Unlike the ANNs, these hyperparameters were explored manually by repeating training runs with different configurations and evaluating performance. The full ranges of hyperparameters considered for both ANNs and U-Nets are provided in Table 6.

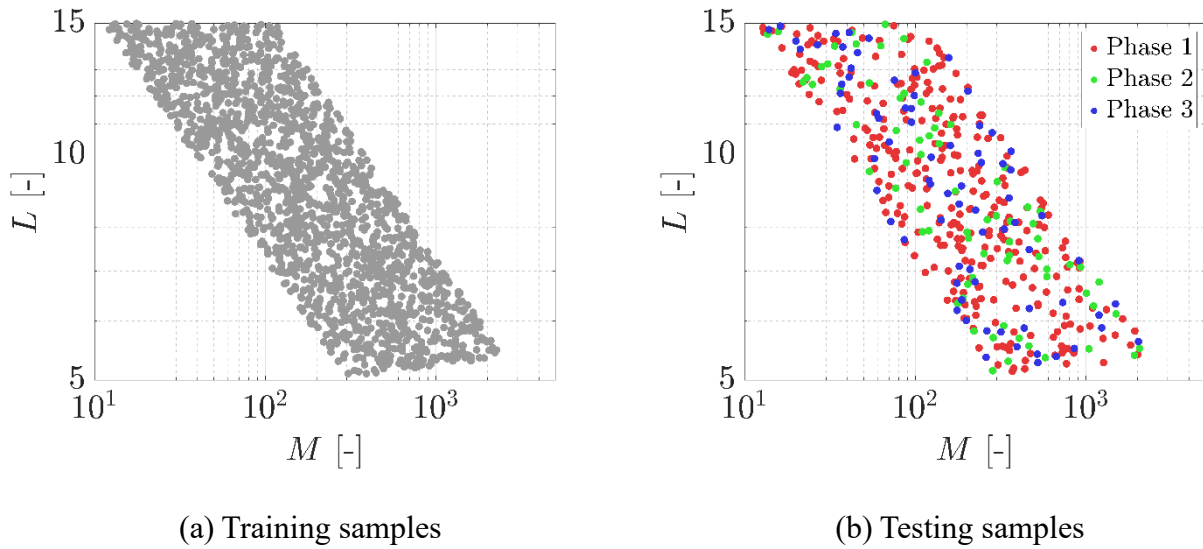
Table 6: Hyperparameter ranges.

Network	Parameter	Range
ANN	Number of hidden layers	1-5
	Number of hidden layer neurons	16-512
	Dropout layer probability	0.01-0.5
U-Net	Encoder depth	3-5
	Number of first encoder filters	16-64

3. Results and discussion

3.1. Training and testing data

Figure 2 shows the parameter space covered by the training and testing samples in this study. The Moes dimensionless parameters for the dataset range from about 5 to 15 for M and from about 10 to 1100 for L . Since all values of L are significantly greater than unity, the simulations lie entirely within the piezoviscous regime. The selected range of M corresponds to elastic behaviour rather than the rigid asymptotic limit. Consequently, all samples fall within the elastic–piezoviscous regime as classified by Moes [33] and later by Nijenbanning et al. [34]. This regime is representative of practical EHL contacts encountered in engineering applications.



327 *Figure 2 – Distribution of all training and testing samples in the Moes parameter space, defined by the*
 328 *dimensionless load parameter (M) and speed parameter (L).*

329

330 Figure 3 highlights the PSD distributions of the rough surfaces used in the training and in the three testing
 331 phases. The PSDs are separated in the x- and y-directions to highlight anisotropic effects. For the training
 332 and Phase 1 testing samples, the PSD curves largely overlap. This is expected since both datasets consist
 333 of Gaussian isotropic surfaces with identical statistical roughness parameters. Although the individual
 334 profiles differ due to random generation, their spectral content remains statistically consistent, resulting in
 335 similar distributions in both spatial directions.

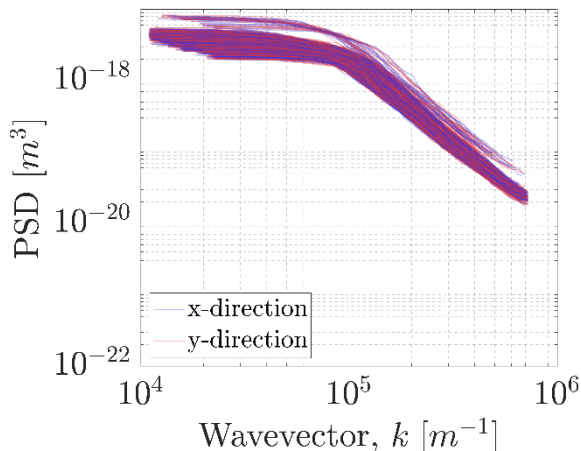
336

337 In Phase 2, where the Peklenik number (γ) is varied, a clear change in anisotropy is observed. Since the
 338 correlation length in the x-direction is kept constant, the PSD curves in the x-direction remain largely
 339 unchanged compared to Phase 1. However, the correlation length in the y-direction does vary, leading to a
 340 noticeable spreading of the PSD curves along that direction. This behaviour confirms that in Phase 2,
 341 anisotropy is introduced while preserving the underlying roughness amplitude.

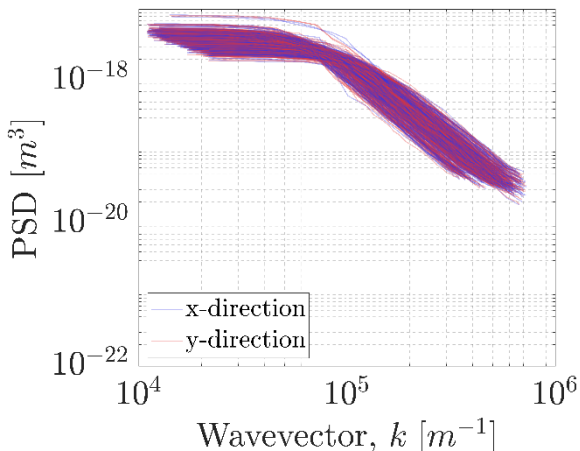
342

343 Lastly, in Phase 3, where the RMS roughness is varied, the overall shape of the PSD curves remains similar
 344 to Phase 1, indicating that the spatial frequency content is preserved. However, the vertical spread of the

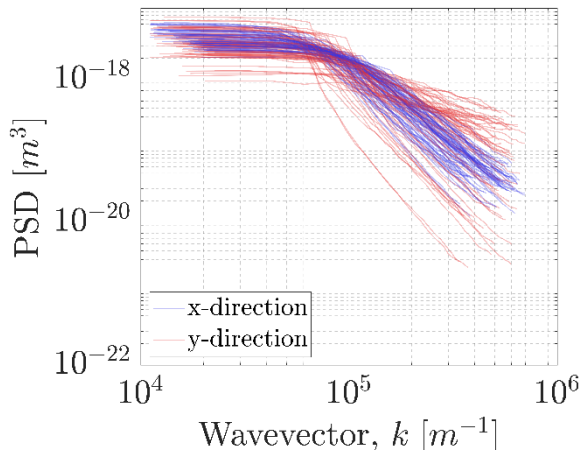
345 PSD curves is increased due to the variation in RMS roughness. This is expected, since the PSD amplitude
 346 scales with the square of surface height [31].



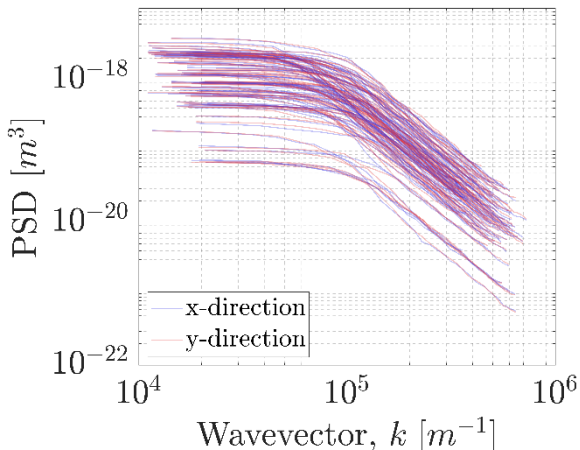
(a) Training samples



(b) Phase 1 testing samples



(c) Phase 2 testing samples



(d) Phase 3 testing samples

347 Figure 3 – Power spectral density (PSD) distributions of the rough surfaces used for training and testing.

348 3.2. Neural network hyperparameters

349 The results of the Bayesian optimisation for the ANN hyperparameters are presented in Table 7.

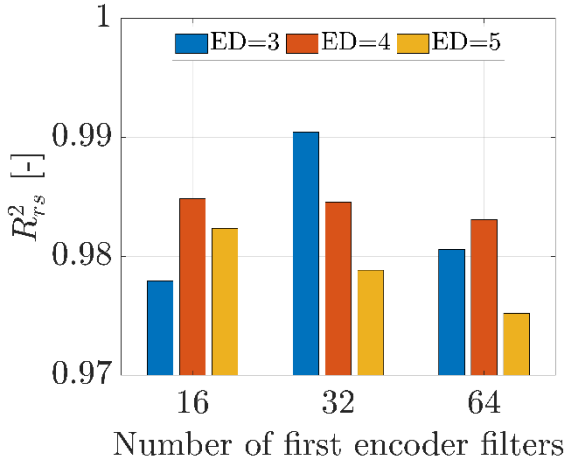
350

351 Table 7: Optimal ANN hyperparameters.

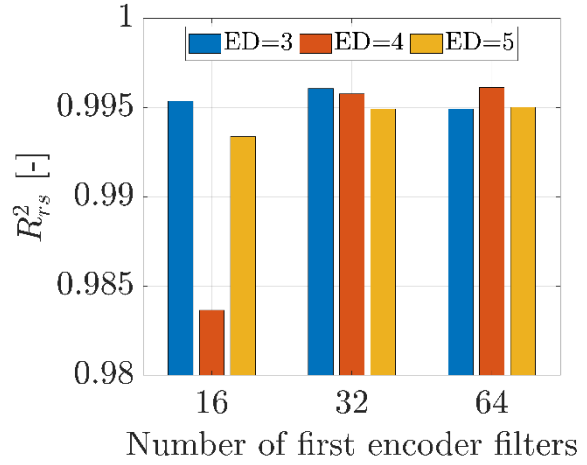
Parameter	ANN		
	Pressure	Film thickness	Temperature
Number of hidden layers	2	5	3
Number of neurons in each layer	256, 256	32, 512, 64, 128, 32	512, 64, 32
Dropout layer probability	0.1244	0.0510	0.0314

352

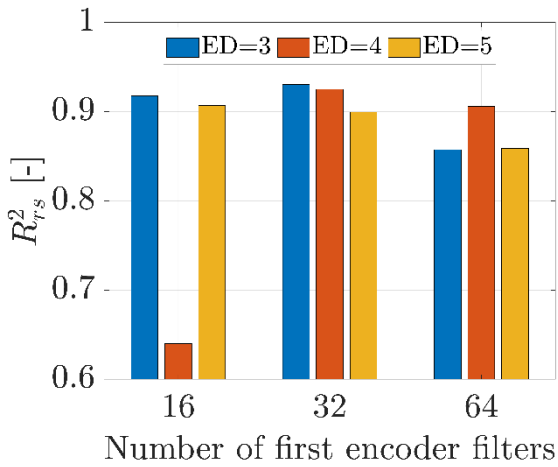
353 Figure 4 shows the effect the encoder depth (ED) and number of first encoder filters have on the mean
354 accuracy of the U-Net predictions. The film thickness results are reported separately for the full profile and
355 for the Hertzian region. This distinction is made because, as mentioned earlier, the macroscopic geometry
356 component of the film thickness profiles was removed prior to training, allowing the network to focus on
357 learning the roughness-induced variations within the contact region where predictive accuracy is most
358 critical.



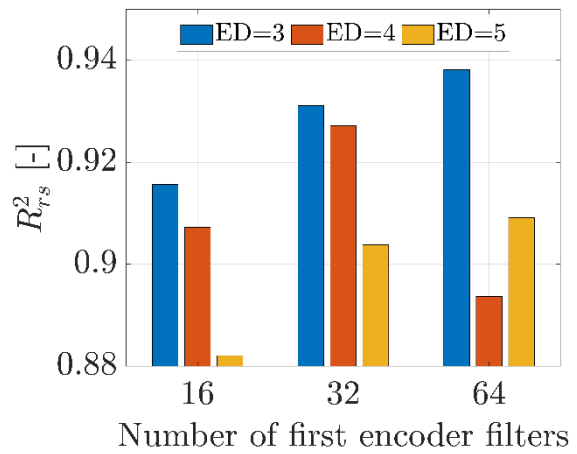
(a) Pressure



(b) Film thickness (full profile)



(c) Film thickness (Hertzian region)



(d) Temperature

Figure 4 – Effect of number of first encoder filters on U-Net mean prediction accuracy.

The results show that both the encoder depth and number of first encoder filters have some influence on the prediction accuracy, although that varies across the different fields. When using an encoder depth of 3, the optimal number of first encoder filters is 32 for pressure and for the Hertzian region film thickness results. For temperature, further increasing the number of first encoder filters to 64 results to a better mean prediction accuracy. This particular trend could be explained by the fact that the pressure and film thickness fields are less complex, being two-dimensional profiles, thus the prediction performance saturates once a sufficient number of first encoder filters is reached. However, the temperature fields require more first encoder filters due to their higher dimensionality, being three-dimensional profiles.

369 For an encoder depth of 4, the mean prediction accuracy for pressure is decreasing with an increasing
370 number of first encoder filters, while for both Hertzian region film thickness and temperature results, the
371 prediction accuracy is highest when the number first encoder filters is 32. Interestingly, there seems to be
372 an outlier result for film thickness when the encoder depth is 4 and the number of first encoder filters is 16.
373 This could be an artefact of the stochastic nature of neural network training and the imposing of early
374 stopping of training to avoid overfitting of data, which occurs when the validation loss flatlines for 30
375 consecutive iterations.

376

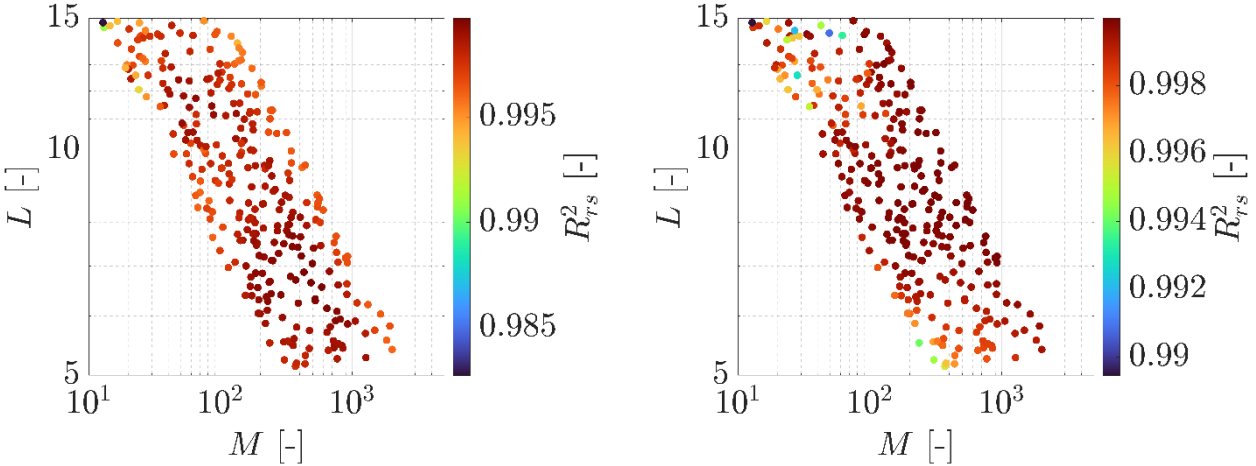
377 For an encoder depth of 5, the mean prediction accuracy for pressure and Hertzian region film thickness is
378 decreasing with an increasing number of first encoder filters, while for the temperature field, the opposite
379 is true as the mean prediction accuracy is increasing with an increasing number of first encoder filters.

380

381 Overall, an encoder depth of 3 seems to results to the most accurate predictions across all fields. With a
382 64×64 mesh, using an encoder depth of 4 or 5 generally results to lower prediction accuracy likely due
383 to excessive downsampling which reduces the spatial resolution required to resolve the localised asperity-
384 induced features. Based on these results, an encoder depth of 3 was used for all three U-Nets, with the
385 number of first encoder filters being 32 for the pressure and film thickness U-Nets and 64 for the
386 temperature U-Net.

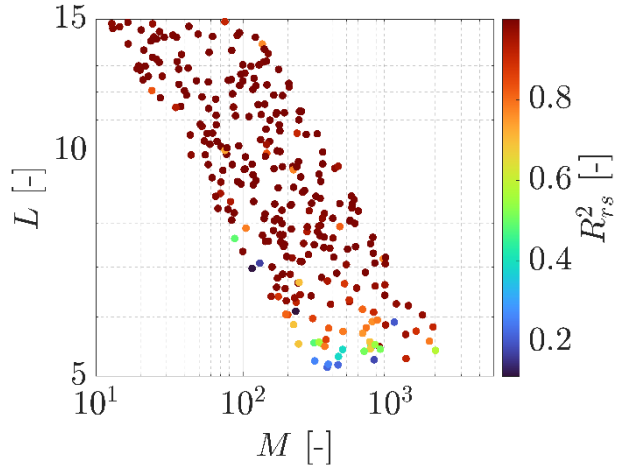
387 3.3. Accuracy of ANN predictions

388 Figure 5 shows the prediction accuracy of the ANNs, in terms of R_{rs}^2 , for smooth pressure, film thickness
 389 and temperature profiles. The mean R_{rs}^2 values are 0.998, 0.999 and 0.925 respectively. The corresponding
 390 mean root mean square error (RMSE) values are 0.014 GPa, 16.546 nm and 0.870 °C.



(a) Pressure (mean $R_{rs}^2 = 0.998$)

(b) Film thickness (mean $R_{rs}^2 = 0.999$)



(c) Temperature (mean $R_{rs}^2 = 0.925$)

Figure 5 – Phase I ANN prediction accuracy.

391
 392
 393 The temperature predictions exhibit slightly reduced accuracy at lower values of L . Since lower L values
 394 correspond to lower entrainment speeds, the magnitude of the temperature rise in these cases is smaller. As
 395 highlighted in the previous study [12] there is a direct correlation between temperature profile magnitude

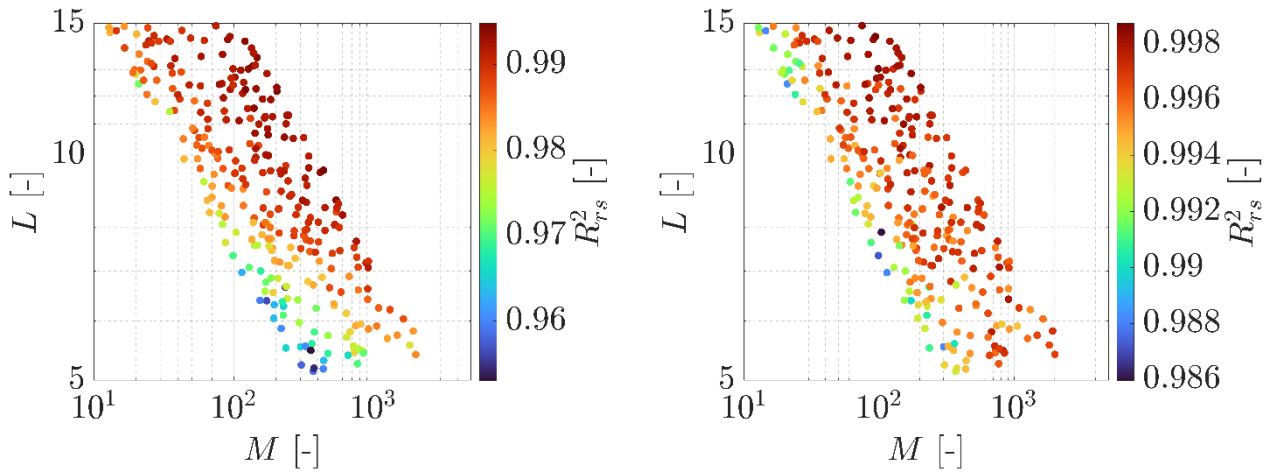
396 and prediction accuracy, with higher magnitude profiles being implicitly prioritised during ANN training.
397 Consequently, reduced temperature gradients at low L values lead to slightly lower predictive performance.
398
399 Compared to that previous study [12], the prediction accuracy of the ANNs is now higher for all three
400 smooth profiles. Previously the reported R_{rs}^2 values were 0.997, 0.997 and 0.873 for pressure, film thickness
401 and temperature, respectively. The observed improvement in the current work can be attributed to two
402 primary factors. First, the number of input parameters has been reduced from twelve to three, simplifying
403 the mapping between inputs and outputs. Second, the present dataset is restricted to the piezoviscous-elastic
404 regime, whereas the earlier study included both piezoviscous-elastic and piezoviscous-rigid regimes.
405 Limiting the parameter space to a single regime reduces variability in the underlying physical behaviour,
406 thereby facilitating more accurate learning by the ANNs.

407

408 3.4. Accuracy of U-Net predictions

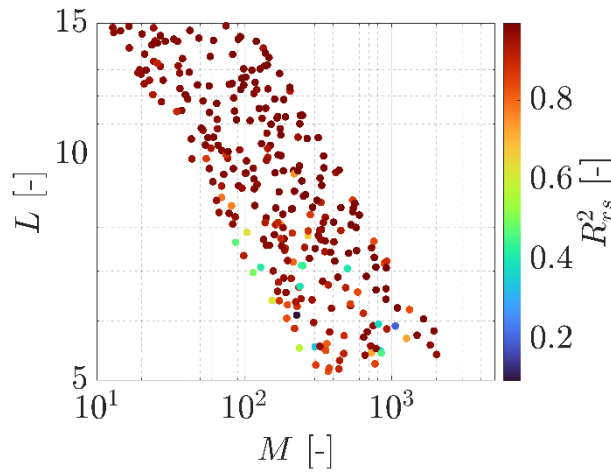
409 3.4.1 Phase 1

410 Figure 6 shows the prediction accuracy of the U-Nets for rough pressure, film thickness and temperature
411 profiles. The mean R_{rs}^2 values are 0.990, 0.996 and 0.938 respectively with the corresponding mean RMSE
412 values are 0.046 GPa, 49.544 nm and 1.510 °C.



(a) Pressure (mean $R_{rs}^2 = 0.990$)

(b) Film thickness (mean $R_{rs}^2 = 0.996$)



(c) Temperature (mean $R_{rs}^2 = 0.938$)

Figure 6 – Phase I U-Net prediction accuracy.

413

414

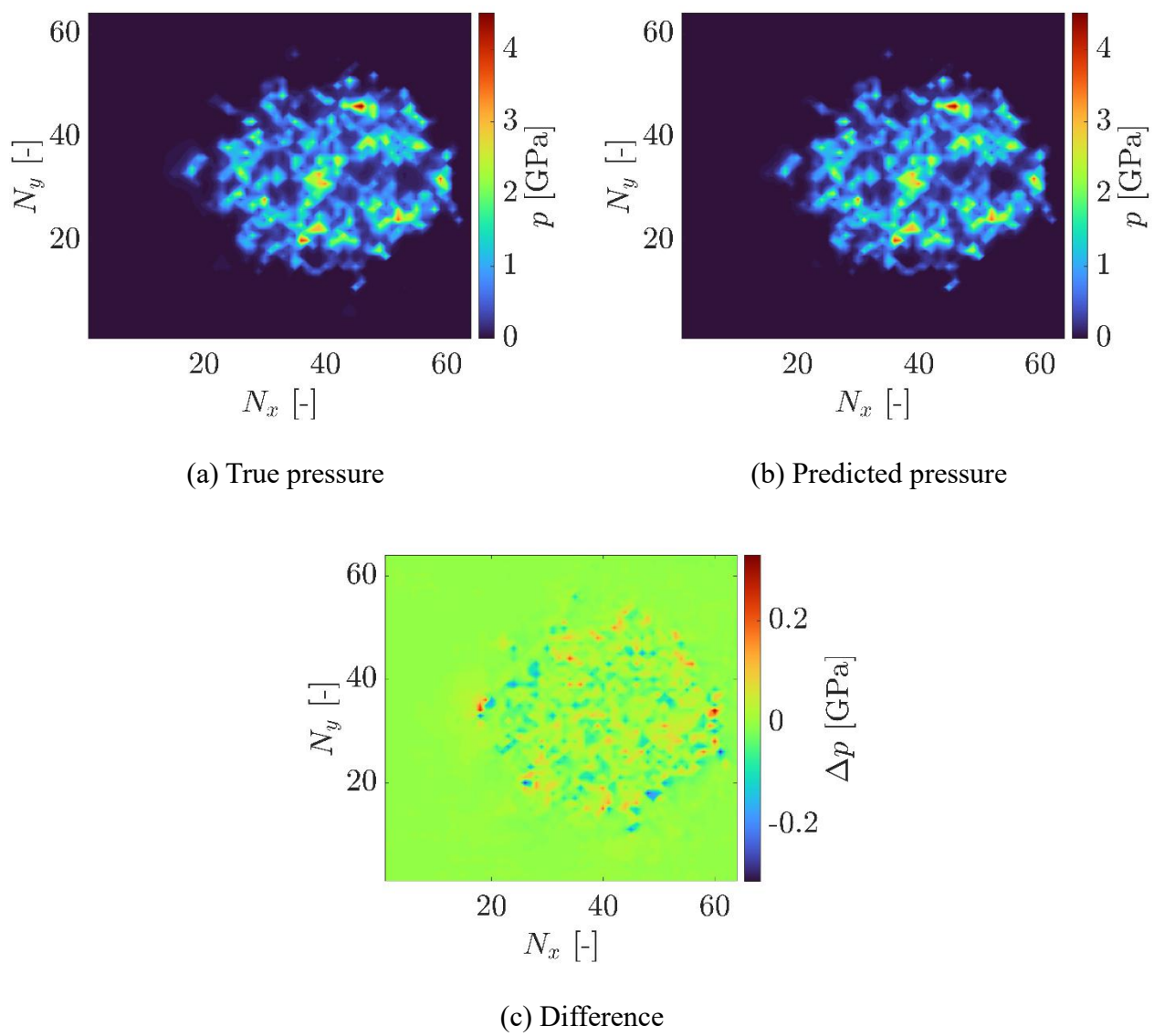
415 Despite the significantly increased spatial complexity of the rough profiles compared to the smooth
 416 solutions, the U-Nets achieve high predictive accuracy across all three output fields. This demonstrates that
 417 the networks successfully learn the nonlinear mapping between the smooth solution, the imposed roughness
 418 distributions and the resulting rough mixed lubrication response.

419

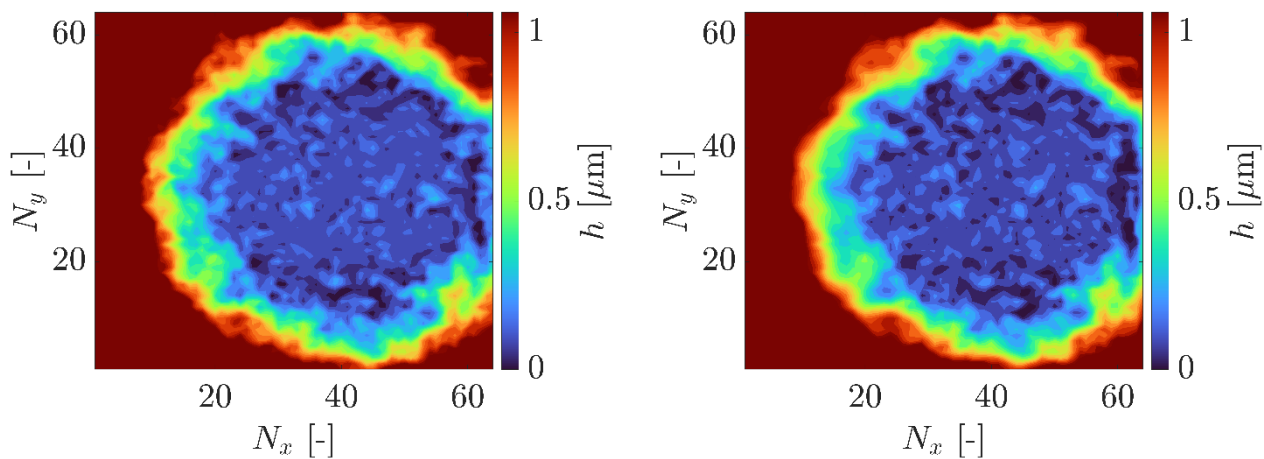
420 Representative examples of classical mixed lubrication solver and U-Net-predicted rough profiles for
 421 pressure, film thickness and mid-film temperature are shown in Figure 7, Figure 8 and Figure 9 respectively.

422 The predicted profiles closely reproduce both the global structure of the contact as well as the roughness-

423 induced fluctuations. In particular, the location and magnitude of local pressure peaks, film thickness
424 perturbations and temperature variations are well captured, confirming that the U-Nets preserve both the
425 macroscopic and microscopic features of the solution.

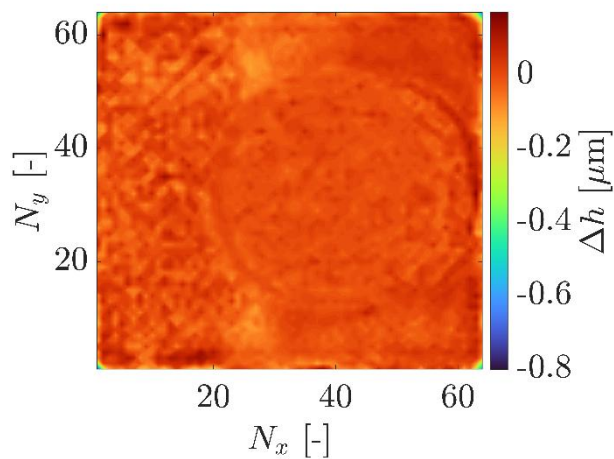


426 *Figure 7 – Example U-Net pressure prediction ($R_{r_s}^2 = 0.995$, $RMSE = 0.036$ GPa).*



(a) True film thickness

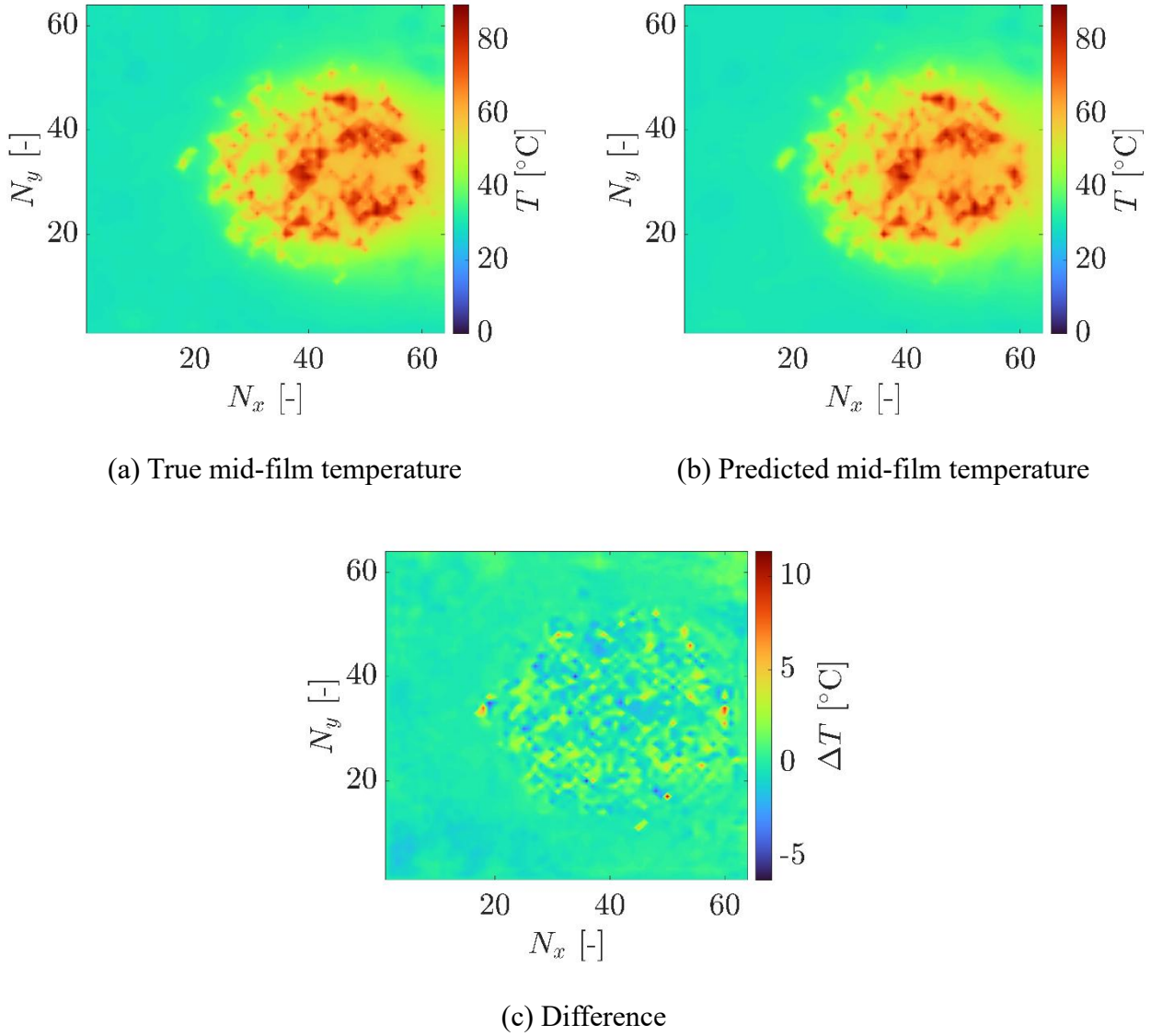
(b) Predicted film thickness



(c) Difference

427

Figure 8 – Example U-Net film thickness prediction ($R_{r_s}^2 = 0.997$, $RMSE = 46.254$ nm).



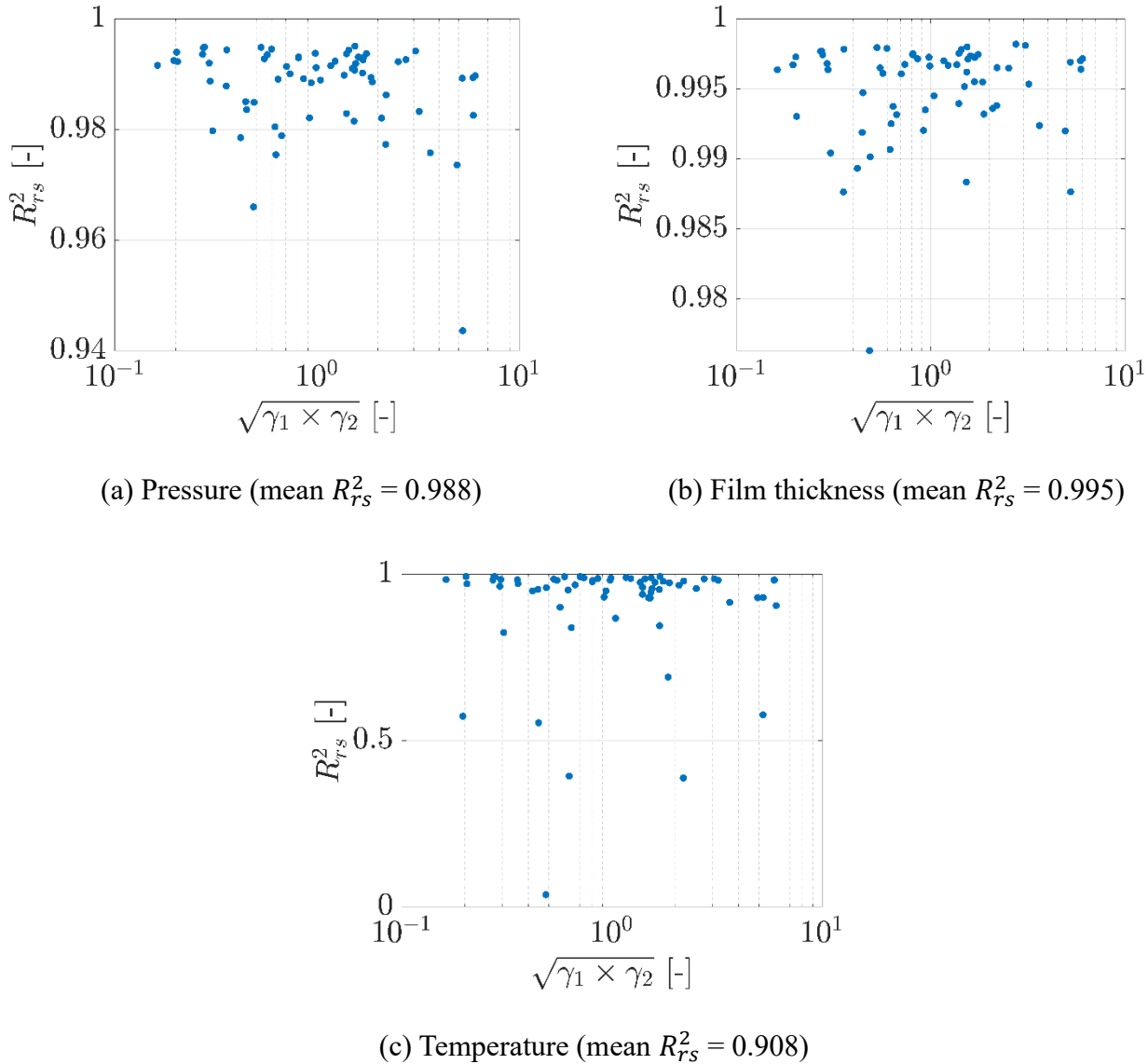
428 *Figure 9 – Example U-Net mid-film temperature prediction ($R_{rs}^2 = 0.993$, $RMSE = 1.031$ $^{\circ}\text{C}$).*

429

430 As expected, the prediction accuracy for temperature is lower than for pressure and film thickness. The
 431 temperature field exhibits stronger localised gradients and is influenced by coupled thermal effects, making
 432 it inherently more difficult to reconstruct accurately. Nevertheless, the R_{rs}^2 value of 0.938 confirms that the
 433 multiscale structure of the rough temperature field is well captured. The overall performance in Phase 1
 434 indicates that the U-Net architecture is capable of accurately reconstructing rough mixed lubrication fields
 435 when the testing samples are drawn from the same statistical roughness distribution as the training dataset.

436 3.4.2 Phase 2

437 Figure 10 shows the prediction accuracy of the U-Nets for rough pressure, film thickness, and temperature
 438 profiles as a function of the combined Peklenik number ($\gamma = \sqrt{\gamma_1 \times \gamma_2}$) of the top and bottom surfaces,
 439 which characterises surface anisotropy. The mean R_{rs}^2 values are 0.988, 0.995 and 0.908 respectively with
 440 the corresponding mean RMSE values being 0.051 GPa, 45.189 nm and 1.561 °C. These results indicate
 441 that the networks maintain high predictive accuracy even when applied to surfaces with varying degrees of
 442 anisotropy, demonstrating good generalisation beyond the isotropic roughness distributions used during
 443 training.



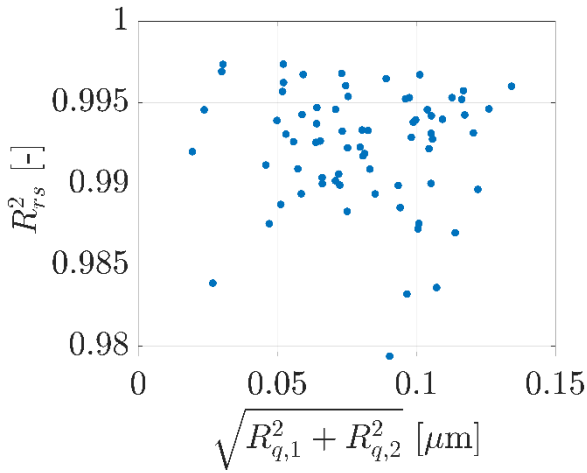
444 *Figure 10 – Phase 2 U-Net prediction accuracy.*

445 As in Phase 1, the temperature predictions remain slightly less accurate than pressure and film thickness.
446 This is due to the stronger localised gradients and nonlinear coupling in the temperature field, which are
447 further amplified by the introduction of anisotropy. The variation in γ modifies the correlation length in the
448 y-direction, generating sharper and more elongated temperature peaks that were not present in the isotropic
449 training data. As a result, while the network captures the overall multiscale structure of the temperature
450 field, fine local variations are harder to reconstruct, leading to a lower accuracy compared to Phase 1.
451 Nevertheless, the predicted profiles reproduce both the global contact structure and the anisotropy-induced
452 local perturbations, confirming that the networks successfully generalise to anisotropic surfaces.

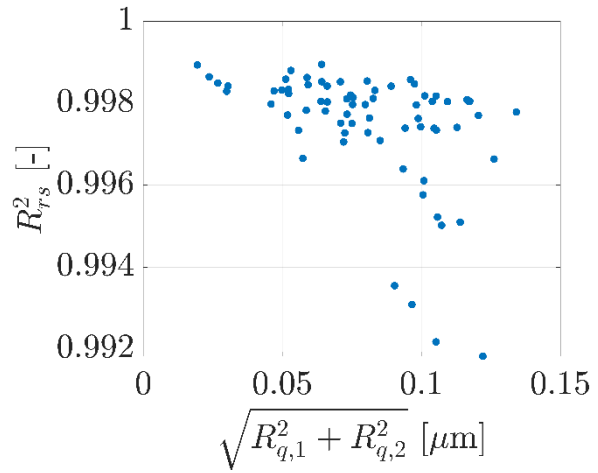
453

454 3.4.3 Phase 3

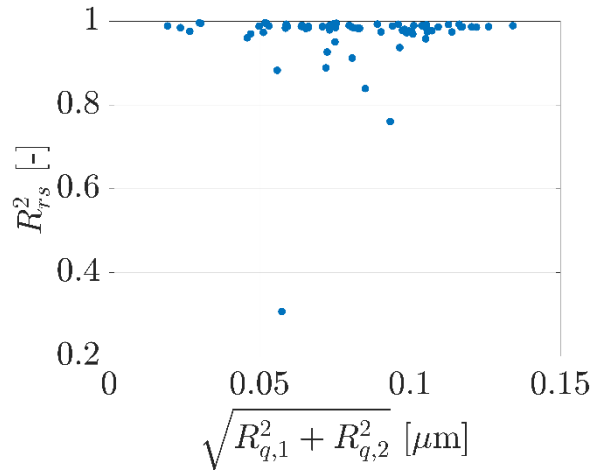
455 Figure 11 shows the prediction accuracy of the U-Nets for rough pressure, film thickness, and temperature
456 profiles as a function of the synthesised RMS roughness. In Phase 1, all surfaces had a fixed RMS of 0.1
457 μm , whereas in Phase 3 the RMS was varied from 0.01 μm to 0.1 μm , representing surfaces with different
458 roughness amplitudes. The mean R_{75}^2 values across all tested RMS values are 0.992, 0.997, and 0.965 for
459 pressure, film thickness, and temperature, respectively with corresponding mean RMSE values being 0.032
460 GPa, 33.663 nm, and 1.145 $^{\circ}\text{C}$.



(a) Pressure (mean $R_{rs}^2 = 0.992$)



(b) Film thickness (mean $R_{rs}^2 = 0.997$)



(c) Temperature (mean $R_{rs}^2 = 0.965$)

Figure 11 – Phase 3 U-Net prediction accuracy.

461

462

463 These results demonstrate that the U-Nets can also generalise to surfaces with different RMS roughness
 464 values than those used during training, maintaining high predictive accuracy across all three output fields.

465 In these figures, there is no clear trend of accuracy with RMS roughness. However, the least accurate film
 466 thickness predictions are occasionally found at higher RMS roughness values (right-hand side of the graph),

467 suggesting that surfaces with larger roughness amplitudes can produce local features that are more
 468 challenging to reconstruct. Notably, the temperature predictions are slightly improved compared to Phase

469 1, likely because the inclusion of surfaces with smaller RMS roughness values introduces smoother local
 470 gradients, allowing the network to more accurately capture the multiscale thermal features.

471 Overall, Phase 3 confirms that the trained U-Nets can interpolate and extrapolate rough mixed lubrication
 472 responses across a range of amplitudes, providing robust predictions for surfaces with different roughness
 473 characteristics than those in the training dataset.

474
 475 3.5. Accuracy of hybrid framework solutions

476 Table 8 presents a summary of the mean accuracy and RMSE values of all the hybrid frameworks in Phase
 477 1 of this study, with the Hybrid FW 3 values corresponding to the U-Net predictions discussed previously.
 478 It should be noted that the accuracy values for Hybrid FW 3 reported here differ slightly from those
 479 presented earlier for the standalone U-Net predictions. This is because a small number of simulations
 480 exhibited convergence difficulties for certain hybrid frameworks. These samples were excluded from the
 481 accuracy calculations and from the subsequent acceleration analysis to ensure a consistent and fair
 482 comparison across all hybrid frameworks. All reported accuracy and acceleration metrics are therefore
 483 based solely on samples for which global convergence was achieved for every framework considered.

484
 485 Table 8: Mean accuracy and RMSE of Phase 1 hybrid framework solutions.

Framework	Mean accuracy, R_{rs}^2			Mean $RMSE$		
	p [-]	h [-]	T [-]	p [GPa]	h [nm]	T [°C]
Hybrid FW 1	1.000	1.000	0.999	0.001	0.135	0.162
Hybrid FW 2	1.000	1.000	0.986	0.007	0.467	0.573
Hybrid FW 3	0.990	0.995	0.939	0.046	44.981	1.538
Hybrid FW 1 (+ ANN)	1.000	1.000	0.978	0.002	0.740	0.315
Hybrid FW 2 (+ ANN)	1.000	1.000	0.965	0.007	0.883	0.712
Hybrid FW 3 (+ ANN)	0.990	0.995	0.921	0.046	45.275	1.582

486
 487 Overall, the hybrid frameworks achieve extremely high levels of agreement with the classical solutions.
 488 The pressure and film thickness predictions remain almost perfectly accurate across all frameworks, with
 489 R_{rs}^2 values close to 1.000 and extremely small RMSE values. This indicates that the neural network

490 predictions provide an excellent initial approximation for these fields, which are either preserved or only
491 minimally corrected during the subsequent numerical iterations.

492

493 As expected, the highest level of agreement with the classical framework is obtained for Hybrid FW 1 and
494 Hybrid FW 1 (+ANN), where both the smooth and rough iterations are allowed to converge fully. In these
495 cases, the pressure and film thickness predictions are effectively identical to the classical solutions, while
496 the temperature fields also maintain very high accuracy with very small RMSE values. In the previous study
497 [12] it was shown that when the simulations were allowed to run to completion after the NN predictions,
498 the converged solutions were identical to those obtained using the classical framework. In the present study,
499 however, this is not strictly the case for the Hybrid FW 1 and Hybrid FW 1 (+ANN) solutions. These small
500 discrepancies compared to the Classical FW are likely related to the less stringent temperature convergence
501 criterion used in the current study (1×10^{-4} compared to 1×10^{-5} in [12]), which may allow small deviations
502 introduced by the neural network predictions to persist in the final converged solution.

503

504 When the rough iteration is limited to a single global iteration in Hybrid FW 2 and Hybrid FW 2 (+ ANN),
505 the pressure and film thickness predictions remain largely unaffected, but a small reduction in temperature
506 accuracy is observed. This is reflected in the reduced R_{rs}^2 values and increased RMSE values for
507 temperature compared to Hybrid FW 1, indicating that a single iteration is not always sufficient to fully
508 correct the discrepancies present in the U-Net-predicted temperature field.

509

510 The lowest accuracy is observed for Hybrid FW 3 and Hybrid FW 3 (+ANN), where the rough iteration is
511 skipped entirely and the U-Net prediction is used directly as the final solution. While the pressure and film
512 thickness predictions remain reasonably accurate, the temperature predictions exhibit a more noticeable
513 reduction in accuracy. This highlights the importance of the subsequent iterative solver acting as a
514 correction step for refining the temperature NN predictions.

515 Overall, these results demonstrate that the hybrid frameworks can maintain extremely high predictive
 516 accuracy while reducing the computational effort associated with solving the rough mixed lubrication
 517 problem. The classical iterative stages play an important role in correcting the neural network predictions,
 518 particularly for the temperature field, while the pressure and film thickness fields appear to be captured
 519 very accurately even with minimal iterative refinement.

520

521 3.6. Simulation time comparison

522 Table 9 summarises the mean simulation times obtained for all frameworks in Phase 1, together with the
 523 percentage reduction relative to the classical framework. The classical framework results to a mean
 524 simulation time of 10.36 minutes across all samples.

525

526 Table 9: Summary of Phase 1 simulation times.

Framework	Mean simulation time, t_{mean} [minutes]	Mean simulation time % difference compared to Classical FW
Classical FW	10.36	-
Hybrid FW 1	9.39	-7.17
Hybrid FW 2	7.89	-22.13
Hybrid FW 3	4.20	-58.03
Hybrid FW 1 (+ ANN)	6.98	-29.95
Hybrid FW 2 (+ ANN)	5.93	-40.11
Hybrid FW 3 (+ ANN)	2.65	-72.85

527

528 All hybrid frameworks provide a reduction in mean simulation time compared to the classical framework.
 529 The smallest improvement is observed for Hybrid FW 1, which reduces the mean simulation time by 7.17%.
 530 This relatively modest reduction is expected since the numerical solver is still allowed to converge fully
 531 during both the smooth and rough iterations.

532 A larger reduction in simulation time is achieved for Hybrid FW 2, where the rough iteration is limited to
533 a single global iteration. In this case, the mean simulation time decreases to 7.89 minutes, representing a
534 22.13% reduction. The reduced number of iterations limits the computational cost while maintaining high
535 solution accuracy, as shown in the previous section.

536

537 The most significant improvement among the frameworks without ANN acceleration is obtained for Hybrid
538 FW 3, where the rough iteration is skipped entirely and the U-Net prediction is used directly as the final
539 rough solution. This reduces the mean simulation time to 4.20 minutes, representing a 58.03% decrease
540 relative to the classical framework. This indicates that, on average, about 42% of the simulation time is
541 spent on the smooth iteration, highlighting that the smooth solver accounts for a substantial portion of the
542 total computational cost even when the rough iteration is fully bypassed.

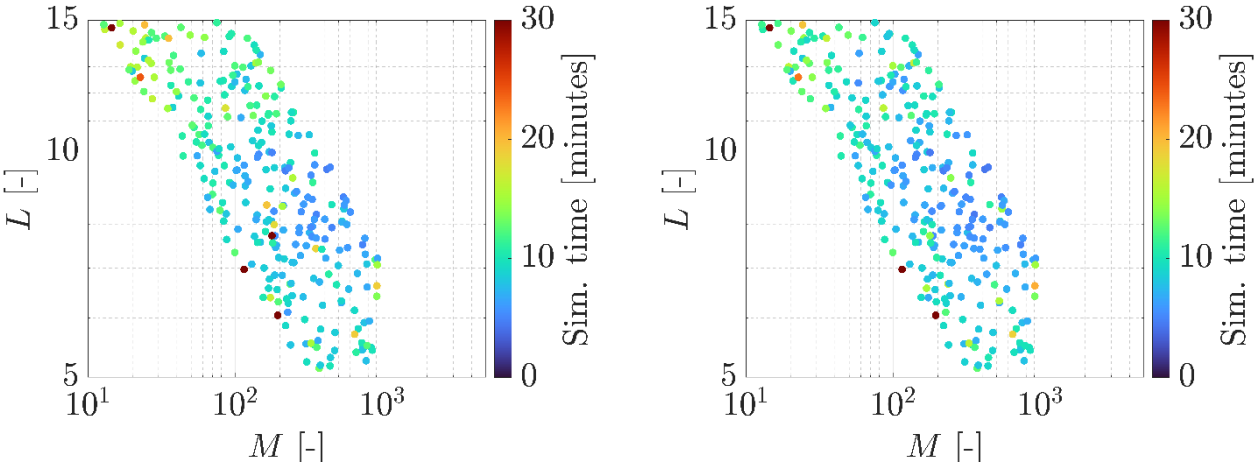
543

544 When the ANN predictions are incorporated into the framework, further reductions in simulation time are
545 achieved. Hybrid FW 1 (+ANN) reduces the mean simulation time by 29.95%, while Hybrid FW 2 (+ANN)
546 achieves a reduction of 40.11%. The largest decrease is obtained for Hybrid FW 3 (+ANN). In this case,
547 the mean simulation time decreases to 2.65 minutes, corresponding to a reduction of 72.85% relative to the
548 classical framework.

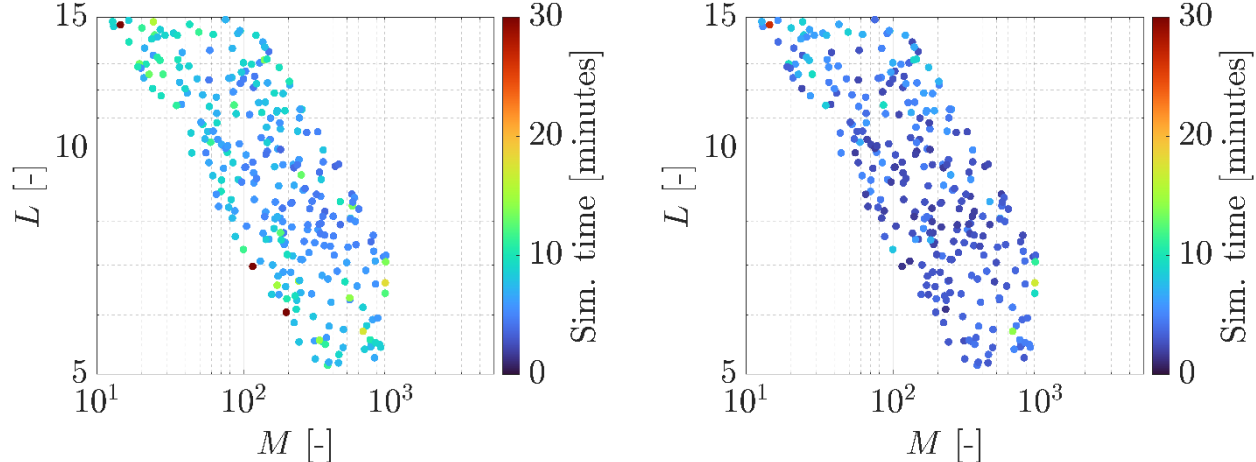
549

550 Figure 12 and Figure 13 provide a more detailed view of the simulation times across the Moes parameter
551 space for hybrid frameworks without and with ANN acceleration, respectively. For the classical framework,
552 simulation times generally increase with L , which is consistent with the previous study [12]. This trend
553 arises because higher L values correspond to higher maximum temperatures in the contact, meaning the
554 initial smooth solution is further from the final converged state, hence more iterations are required to reach
555 convergence. Interestingly, a few simulations in the classical framework exhibit extreme simulation times
556 which persist in Hybrid FW 1 and Hybrid FW 2. These outliers highlight cases where the rough iteration is
557 particularly slow. In contrast, Hybrid FW 3 and Hybrid FW 3 (+ANN), which entirely replace the rough

558 iteration with U-Net predictions, largely eliminate these extreme cases, demonstrating that the U-Net
 559 predictions effectively bypass the most computationally expensive stages of the solver.

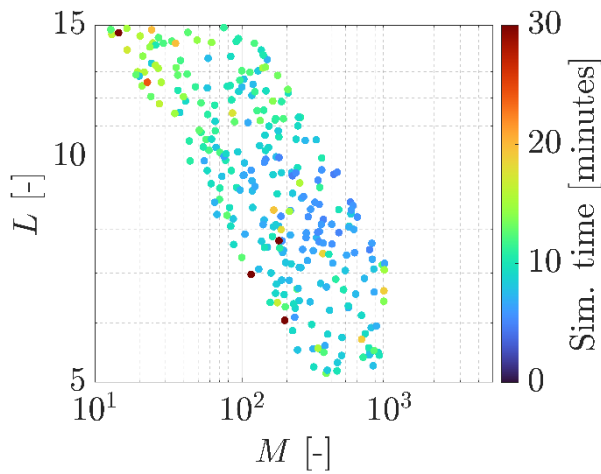


(a) Classical FW (mean $t = 10.36$ minutes) (b) Hybrid FW 1 (mean $t = 9.39$ minutes)

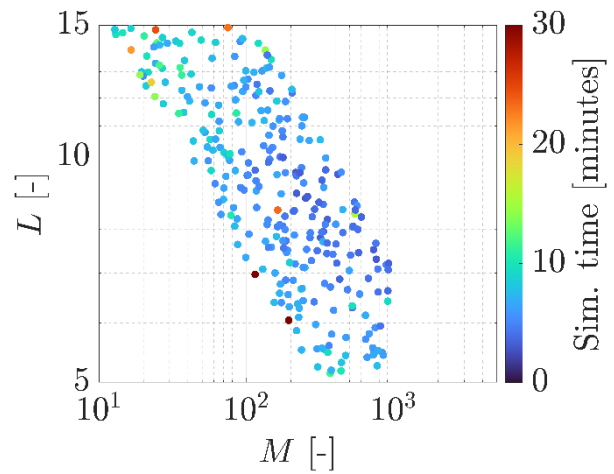


(c) Hybrid FW 2 (mean $t = 7.89$ minutes) (d) Hybrid FW 3 (mean $t = 4.20$ minutes)

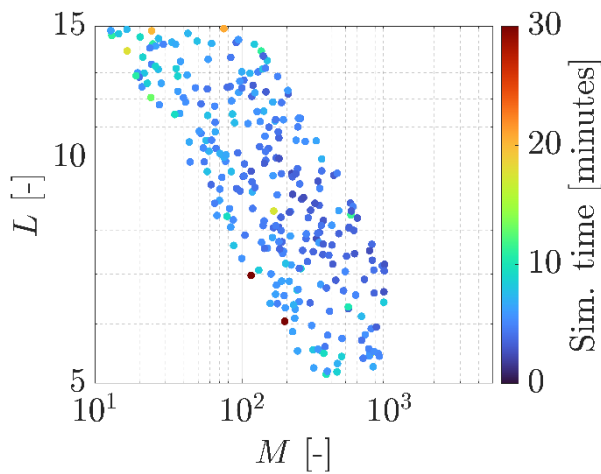
560 *Figure 12 – Simulation times of Phase 1 hybrid frameworks without ANN acceleration.*



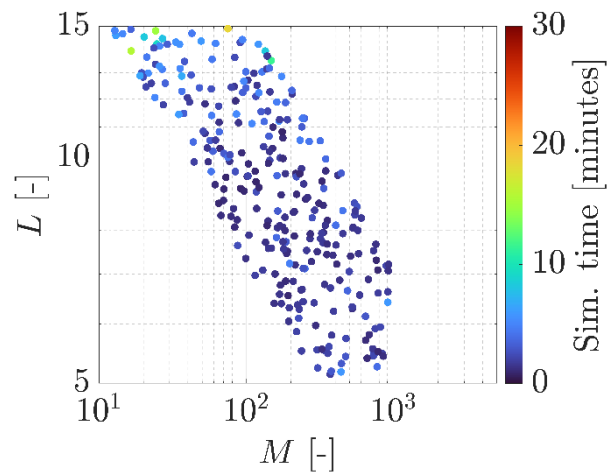
(a) Classical FW (mean $t = 10.36$ minutes)



(b) Hybrid FW 1 (+ANN) (mean $t = 6.98$ minutes)



(c) Hybrid FW 2 (+ANN) (mean $t = 5.93$ minutes)



(d) Hybrid FW 3 (+ANN) (mean $t = 2.65$ minutes)

Figure 13 – Simulation times of Phase I hybrid frameworks with ANN acceleration.

Overall, these results demonstrate that the hybrid frameworks can substantially reduce the computational cost of rough mixed lubrication simulations. The largest reductions are achieved when the neural network predictions replace the most computationally expensive stages of the numerical solver, with only a small impact on solution accuracy, particularly for the temperature field. It should be noted that the simulation times reported for these frameworks represent a “worst-case” scenario, as only two time iterations were performed in this study. In practical applications, where more rough iterations are typically required, the relative time savings for Hybrid FW 3 would likely be even greater.

570 Future work could focus on extending the framework to broader lubrication regimes and more complex,
571 non-Gaussian surface topographies. In particular, improved treatment of thermal effects remains an
572 important direction for enhancing predictive accuracy. This could be achieved through more optimised
573 network architectures or by combining physics-informed training strategies with purely data-driven
574 machine learning methods. While PINNs alone have shown limitations in capturing strongly nonlinear,
575 tightly coupled TEHL behaviour, they may still offer value in ensuring physical consistency of the data-
576 driven predictions.

578 **4. Conclusions**

579 This study has presented a hybrid computational framework for accelerating mixed lubrication simulations
580 through the integration of ANNs and CNNs, specifically U-Nets, within a classical finite volume solver.
581 The methodology extends previous work on smooth TEHL problems to deterministic rough surface
582 conditions by enabling the direct prediction of rough pressure, film thickness and temperature fields.

583
584 A unified finite volume lubrication model was employed as the baseline solver. To address the high
585 computational cost associated with rough surface simulations, particularly due to the gradual introduction
586 of roughness over multiple time steps, a series of hybrid frameworks were developed. These frameworks
587 combine ANN-based prediction of smooth fields and U-Net-based reconstruction of rough fields, with
588 varying levels of reliance on the classical iterative solver. This structure allows for a systematic trade-off
589 between computational efficiency and solution accuracy.

590
591 The ANN models demonstrated high accuracy for smooth TEHL predictions, while the U-Net models
592 achieved strong performance in predicting rough mixed lubrication fields, capturing both global contact
593 behaviour and local roughness-induced perturbations. Pressure and film thickness were consistently
594 predicted with very high accuracy across all test cases, while temperature remained the most challenging
595 field due to its stronger nonlinear coupling and sharper spatial gradients.

596 Overall, the hybrid frameworks achieved substantial reductions in computational cost compared to the
597 classical solver, with the most efficient configuration reducing simulation time by over 70% while
598 maintaining good agreement with high-fidelity solutions. In addition, the hybrid approach mitigated
599 extreme runtime variability associated with convergence issues in the classical solver, highlighting its
600 potential for robust and efficient simulation.

601

602 These results demonstrate that hybrid machine learning–numerical approaches can provide a viable and
603 efficient alternative to conventional mixed lubrication solvers, offering significant computational savings
604 while preserving high predictive accuracy, thus enabling simulation capabilities suitable for real-time
605 engineering applications such as digital twins and online condition monitoring systems.

CRedit authorship contribution statement

Conceptualization, F.K., S.A., D.D. and J.P.E.; Methodology, F.K. and S.A.; Software, F.K. and S.A.; Validation, F.K. and S.A.; Formal Analysis, F.K.; Investigation, F.K.; Resources, D.D. and J.P.E.; Data Curation, F.K.; Writing – Original Draft Preparation, F.K.; Writing – Review and Editing, S.A., D.D and J.P.E.; Visualization, F.K.; Supervision, D.D and J.P.E.; Project Administration, D.D; Funding Acquisition, D.D and J.P.E.

Declaration of competing interest

The authors declare that they have no known competing financial interests or personal relationships that could have appeared to influence the work reported in this paper.

Acknowledgements

F.K. thanks the UK Department of Science, Innovation and Technology (DSIT), the Engineering and Physical Sciences Research Council (EPSRC), and Shell for PhD funding through an iCASE studentship (EP/X524773/1). The authors thank Shell and the EPSRC for funding via the InFUSE Prosperity Partnership (EP/V038044/1). D.D. acknowledges the support of the Royal Academy of Engineering (RAEng) for the Shell/RAEng Research Chair in Complex Engineering Interfaces. J.P.E. acknowledges the support of the RAEng through their Research Fellowships scheme.

References

- [1] Q. J. Wang and D. Zhu, *Interfacial Mechanics*. First edition. | Boca Raton, FL : CRC Press/Taylor & Francis Group, 2019.: CRC Press, 2019. doi: 10.1201/9780429131011.
- [2] H. R. Braun, S. Korres, P. Laurs, and J. W. H. Franke, “Impact of ultra-low viscosity fluids on drivetrain functionality and durability,” *Lubricants*, vol. 9, no. 12, 2021, doi: 10.3390/lubricants9120119.
- [3] G. E. Morales-Espejel, “Surface roughness effects in elastohydrodynamic lubrication: A review with contributions,” 2014. doi: 10.1177/1350650113513572.
- [4] X. Ai and H. S. Cheng, “The Influence of Moving Dent on Point EHL Contacts,” *Tribology Transactions*, vol. 37, no. 2, pp. 323–335, Jan. 1994, doi: 10.1080/10402009408983301.
- [5] L. Chang, “A deterministic model for line-contact partial elastohydrodynamic lubrication,” *Tribol. Int.*, vol. 28, no. 2, pp. 75–84, Mar. 1995, doi: 10.1016/0301-679X(95)92697-4.
- [6] Y.-Z. Hu and D. Zhu, “A Full Numerical Solution to the Mixed Lubrication in Point Contacts,” *J. Tribol.*, vol. 122, no. 1, pp. 1–9, Jan. 2000, doi: 10.1115/1.555322.
- [7] D. Zhu and Y. Z. Hu, “A computer program package for the prediction of ehl and mixed lubrication characteristics, friction, subsurface stresses and flash temperatures based on measured 3-d surface roughness,” *Tribology Transactions*, vol. 44, no. 3, 2001, doi: 10.1080/10402000108982471.
- [8] C. H. Venner and A. A. Lubrecht, “Multilevel methods in lubrication,” *Tribology Series*, vol. 37, 2000, doi: 10.1243/1350650011543727.
- [9] S. Liu, Q. Wang, and G. Liu, “A versatile method of discrete convolution and FFT (DC-FFT) for contact analyses,” *Wear*, vol. 243, no. 1–2, pp. 101–111, Aug. 2000, doi: 10.1016/S0043-1648(00)00427-0.
- [10] S. Ardah, F. J. Profito, T. Reddyhoff, and D. Dini, “Advanced modelling of lubricated interfaces in general curvilinear grids,” *Tribol. Int.*, vol. 188, p. 108727, Oct. 2023, doi: 10.1016/j.triboint.2023.108727.

- 651 [11] S. Ardah, F. J. Profito, and D. Dini, “An integrated finite volume framework for thermal
652 elasto-hydrodynamic lubrication,” *Tribol. Int.*, vol. 177, p. 107935, Jan. 2023, doi:
653 10.1016/j.triboint.2022.107935.
- 654 [12] F. Kaliafetis, S. Ardah, J. P. Ewen, and D. Dini, “Using artificial neural networks to
655 accelerate thermo-elastohydrodynamic lubrication simulations,” *Tribol. Int.*, vol. 212, 2025,
656 doi: 10.1016/j.triboint.2025.110978.
- 657 [13] M. Marian and S. Tremmel, “Current trends and applications of machine learning in
658 tribology—a review,” 2021. doi: 10.3390/LUBRICANTS9090086.
- 659 [14] M. Marian, J. Mursak, M. Bartz, F. J. Profito, A. Rosenkranz, and S. Wartzack, “Predicting
660 EHL film thickness parameters by machine learning approaches,” *Friction*, vol. 11, no. 6,
661 pp. 992–1013, Jun. 2023, doi: 10.1007/s40544-022-0641-6.
- 662 [15] W. Habchi and S. Bair, “Machine-Learning-Assisted Identification and Formulation of
663 High-Pressure Lubricant-Piezoviscous-Response Parameters for Minimum Film Thickness
664 Determination in Elastohydrodynamic Circular Contacts,” *Tribol. Lett.*, vol. 72, no. 4, p.
665 134, Dec. 2024, doi: 10.1007/s11249-024-01937-2.
- 666 [16] J. Kelley, V. Schneider, G. Poll, and M. Marian, “Enhancing practical modeling: A neural
667 network approach for locally-resolved prediction of elastohydrodynamic line contacts,”
668 *Tribol. Int.*, vol. 199, 2024, doi: 10.1016/j.triboint.2024.109988.
- 669 [17] C. Zhang, M. Tošić, J. Kelley, W. Habchi, M. Marian, and T. Lohner, “A Modular and
670 Generalized Machine Learning Approach for Non-Newtonian EHL Film Thickness
671 Prediction,” *Tribol. Int.*, p. 112211, May 2026, doi: 10.1016/j.triboint.2026.112211.
- 672 [18] M. Raissi, P. Perdikaris, and G. E. Karniadakis, “Physics-informed neural networks: A deep
673 learning framework for solving forward and inverse problems involving nonlinear partial
674 differential equations,” *J. Comput. Phys.*, vol. 378, 2019, doi: 10.1016/j.jcp.2018.10.045.

- 675 [19] A. Almqvist, “Fundamentals of Physics-Informed Neural Networks Applied to Solve the
676 Reynolds Boundary Value Problem,” *Lubricants*, vol. 9, no. 8, p. 82, Aug. 2021, doi:
677 10.3390/lubricants9080082.
- 678 [20] M. Marian and S. Tremmel, “Physics-Informed Machine Learning—An Emerging Trend in
679 Tribology,” *Lubricants*, vol. 11, no. 11, p. 463, Oct. 2023, doi: 10.3390/lubricants11110463.
- 680 [21] S. Cuomo, V. S. Di Cola, F. Giampaolo, G. Rozza, M. Raissi, and F. Piccialli, “Scientific
681 Machine Learning Through Physics–Informed Neural Networks: Where we are and What’s
682 Next,” *J. Sci. Comput.*, vol. 92, 2022, doi: 10.1007/s10915-022-01939-z.
- 683 [22] S. Zhao, L. Hou, R. Yang, and G. Zhou, “An adaptively weighted multi-scale physics-
684 informed neural network for elastohydrodynamic lubrication in rough-surface point
685 contacts,” *Tribol. Int.*, vol. 224, p. 112270, Dec. 2026, doi: 10.1016/j.triboint.2026.112270.
- 686 [23] J. Gu *et al.*, “Recent advances in convolutional neural networks,” *Pattern Recognit.*, vol. 77,
687 2018, doi: 10.1016/j.patcog.2017.10.013.
- 688 [24] W. Xu *et al.*, “High-resolution u-net: Preserving image details for cultivated land
689 extraction,” *Sensors (Switzerland)*, vol. 20, no. 15, 2020, doi: 10.3390/s20154064.
- 690 [25] W. Yang, R. Zhang, S. K. K. Chow, and Z. Li, “A survey of U-Net variant network for MRI
691 brain tumor segmentation,” *Discover Artificial Intelligence*, 2025, doi: 10.1007/s44163-025-
692 00525-0.
- 693 [26] C. Bian and X. Chen, “MambaClinix: hierarchical gated convolution and mamba-based u-
694 net for enhanced 3D medical image segmentation,” *Biomed. Signal Process. Control*, vol.
695 124, p. 110657, Sep. 2026, doi: 10.1016/j.bspc.2026.110657.
- 696 [27] B. Feng, S. Lyu, and Y. He, “Brain tumour segmentation using learnable wavelet transform
697 and attention mechanism network,” *Biomed. Signal Process. Control*, vol. 122, p. 110444,
698 Aug. 2026, doi: 10.1016/j.bspc.2026.110444.

- 699 [28] Y. Matsuzaka and M. Iyoda, “Applications, image analysis, and interpretation of computer
700 vision in medical imaging,” *Frontiers in Radiology*, vol. 5, 2026, doi:
701 10.3389/fradi.2025.1733003.
- 702 [29] F. Kaliafetis, D. Dini, J. P. Ewen, and S. Ardah, “A Finite Volume-based Unified Transient
703 Deterministic Framework for Lubrication Modelling,” *engrXiv*, 2026, doi: 10.31224/7085.
- 704 [30] PCS Instruments, “MTM.” Accessed: Apr. 07, 2025. [Online]. Available: [https://pcs-](https://pcs-instruments.com/product/mtm/)
705 [instruments.com/product/mtm/](https://pcs-instruments.com/product/mtm/)
- 706 [31] A. Pradhan *et al.*, “The Surface-Topography Challenge: A Multi-Laboratory Benchmark
707 Study to Advance the Characterization of Topography,” *Tribol. Lett.*, vol. 73, no. 3, 2025,
708 doi: 10.1007/s11249-025-02014-y.
- 709 [32] T. Agrawal, *Hyperparameter Optimization in Machine Learning*. Berkeley, CA: Apress,
710 2021. doi: 10.1007/978-1-4842-6579-6.
- 711 [33] O. Ronneberger, P. Fischer, and T. Brox, “U-net: Convolutional networks for biomedical
712 image segmentation,” in *Lecture Notes in Computer Science (including subseries Lecture*
713 *Notes in Artificial Intelligence and Lecture Notes in Bioinformatics)*, 2015. doi:
714 10.1007/978-3-319-24574-4_28.
- 715 [34] H. Moes, “Optimum similarity analysis with applications to elastohydrodynamic
716 lubrication,” *Wear*, vol. 159, no. 1, pp. 57–66, Nov. 1992, doi: 10.1016/0043-
717 1648(92)90286-H.
- 718 [35] G. Nijebanning, C. H. Venner, and H. Moes, “Film thickness in elastohydrodynamically
719 lubricated elliptic contacts,” *Wear*, vol. 176, no. 2, pp. 217–229, Aug. 1994, doi:
720 10.1016/0043-1648(94)90150-3.
- 721